Journal of Micromechanics and Microengineering

Effect of simultaneous electrical and mechanical stressing on porosity of $Ti_3C_2T_x$ MXene films

OPEN ACCESS
IOP Publishing
Journal of Micromechanics and Microengineering
J. Micromech. Microeng. **33** (2023) 045007 (10pp)
https://doi.org/10.1088/1361-6439/acbfc4

Effect of simultaneous electrical and mechanical stressing on porosity of $Ti_3C_2T_x$ MXene films

Logan C Sharp[1], Nahid Sultan Al-Mamun[1], Maxwell Wetherington[2] and Aman Haque[1,*]

[1] Department of Mechanical Engineering, Penn State University, University Park, PA 16802, United States of America
[2] Materials Characterization Laboratory, Penn State University, University Park, PA 16802, United States of America

E-mail: mah37@psu.edu

Received 6 November 2022, revised 11 February 2023
Accepted for publication 28 February 2023
Published 10 March 2023

Abstract

MXenes are atomically layered carbides and nitrides of transition metals that have potential for micro-devices applications in energy storage, conversion, and transport. This emerging family of materials is typically studied as nanosheets or ultra-thin films, for which the internal defects are mostly nanoscale flake-flake interface separation type. However, micro-devices applications would require thicker films, which exhibit very high density of microscale pores. Electrical conductivity of thicker MXenes is significantly lower than nanosheets, and the physics of defect size and density control are also different and less understood. Current art is to perform high temperature annealing to improve the electrical conductivity, which can structurally alter or degrade MXene. The key contribution of this study is a room-temperature annealing process that exploits the synergy between electrical pulses and compressive mechanical loading. Experimental results indicate over a 90% increase in electrical conductivity, which reflects a decrease in void size and density. In the absence of compressive loading, the same process resulted in a conductivity increase of approximately 75%. Analytical spectroscopy and microscopy indicated that the proposed multi-stimuli process kept the MXene composition intact while significantly decreasing the void size and density.

Keywords: MXene, titanium carbide, annealing, electron wind force

(Some figures may appear in colour only in the online journal)

1. Introduction

Since their discovery in 2011, two-dimensional (2D) layered carbides and nitrides of transition metals, known as MXenes, have rapidly emerged due to their attractive physical properties [1]. MXenes are generally obtained by removing the intermediate element from their MAX phase precursor, which stems from the chemical formula $M_{n+1}AX_n$. Where M denotes a transition metal, A denotes an A-group of elements, X denotes carbon and/or nitrogen, and n denotes the layers of X. They have been touted for mostly energy, electronic, and photonic systems applications, including supercapacitors [2, 3], batteries [3, 4], electromagnetic interference shielding [5, 6], wireless communication [7], water treatment [8], and photonic devices [9]. More recent studies have led to scalable processing, which is required for micro-engineering applications. In addition to conventional photolithography,

* Author to whom any correspondence should be addressed.

the fabrication processing is amenable to other mass production techniques, such as laser scribing, screen printing, stamping, and extrusion printing [10]. An example of micro-electro-mechanical systems (MEMS) integration is the planar interdigital supercapacitor, which has recently been shown to outperform conventional sandwich design in energy density [11]. This is important for co-fabrication of power sources in the same circuit board as the micro-electronic devices. Another impactful application area is sensors, where MXene can be integrated with MEMS devices as the active sensor material [12]. Their attractive gauge factor (∼770) and strain compatibility (30%–130%) implies not just high sensitivity, but also flexibility -required for wearable MEMS sensors [13, 14]. Recently, electrochemical actuators converting electrical energy into mechanical energy have been demonstrated [15]. Further research on the electro-mechanical response will facilitate MXene applications in MEMS and mm scale devices as power generation, sensor, or even actuation units.

While nanoscale MXene flakes show mostly inter-layer defects (hence exhibiting excellent properties), MEMS applications will require thicker (on the order of microns) films. Thick MXene films have high density of microscale pores, bringing significant changes in the physical properties. Therefore, the study of defect characterization and control is important for technological applications. Commonly, thermal annealing [2, 16–19] is performed to improve the MXene properties. However, MXenes undergo structural oxidation and degradation when exposed to high temperatures in an oxygen-containing environment, which results in negative effects on the electrical conductivity [20]. To avoid oxidation, thermal annealing of MXenes has been performed at temperatures of up to 1500 °C in vacuum or inert environments [18, 21, 22]. Overall, thermal annealing is an effective way to alter $Ti_3C_2T_x$, but the required temperatures lead to structural oxidation under ambient conditions [20].

In this study, a non-thermal room temperature (RT) annealing process is presented for $Ti_3C_2T_x$ MXene films that can achieve >90% reduction in electrical resistivity. Throughout this paper, the term 'anneal' is used to describe the reduction or mitigation of defects, even though the formal definition implies the application of high temperatures for a prolonged period of time. The technique requires only electrodes and hence could be compatible with most types of MEMS applications. Here, instead of a DC current, very high current density but low duty cycle pulses are applied. The electrical pulses produce an electron wind force (EWF) when the pulsating high-energy electrons are scattered by defects. In this process, electron momentum is absorbed by the defective regions, giving rise to a mechanical force. The very low duty cycle of the pulses implies that Joule heating is dissipated, and there is minimal or no increase in temperature. In addition to the electrical pulses, we investigate the effect of simultaneous compressive mechanical loading. The concept behind compressive loading is to close the pores inside the specimens as much as possible to maximize the electrical contact between the flakes that constitute the sample. Our hypothesis is that compressed pores with increased electrical contact will allow efficient generation of EWF, which mobilizes the defects to influence their size and density. To compare the effectiveness of compressive loading, these results were compared with those of samples annealed using electropulsing only. The proposed process takes place at RT and has the unique advantage that it can be completed in ambient environments without oxidation. It is important to note that the inherently low temperature of this technique makes it very different compared to rapid thermal annealing (RTA). RTA is performed at temperatures higher than 1000 °C [23], whereas this process can take place at RT. It is a well-established technique for annealing and activation in ion implantation and improved contacts formation. It has also been applied for a broad variety of applications such as oxidation, chemical vapor deposition, phase change, and residual stress.

2. Experimental methods

The as-received $Ti_3C_2T_x$ MXene film was obtained with a diameter of 50 mm and thickness of 500 μm from Nanochemazone, as shown in figure 1(a). The circular spots in the specimen were due to the vacuum packaging on the patterned substrate. Small coupons were cut from a large specimen without including any spot features. The smaller, rectangular-shaped samples were mounted on card stock substrates, as a low thermal conductivity substrate (approximately 0.05 W mK^{-1}) is suitable for the annealing process. Electrical connections were made using silver epoxy. A Northrop Grumman eDrive laser system controller diode-based pulsing instrument was used to generate a DC pulse current. The eDrive was powered by a Sorensen DCS 100–12E power supply set to 20 V DC. The electrical signal generated by the eDrive was characterized using a Rigol DS 1104 oscilloscope. For all experiments, the electrical signal generated from eDrive consisted of a peak current of up to 15 A, a frequency of 2 Hz, and a pulse-width of 40 μs. The current density, pulse-width, and duty cycle values were chosen after performing preliminary experiments with the objective of appreciable decrease in resistivity without any rise in temperature. Higher current density results in higher EWF, but also at the cost of potentially higher Joule heating. Smaller pulse-width ensures minimal temperature rise because phonon speed is slower than electrons, while the smaller duty cycle allows enough time for heat dissipation. A visual representation of the electrical signal is shown in figure 1(b). The eDrive was also used to sense the electrical current during electropulsing. This sensed current was used to calculate the resulting current densities through the samples during the annealing. Electropulsing was performed for only 4 min for all samples. To compress the $Ti_3C_2T_x$ MXene samples during electropulsing, a three-dimensional (3D) printed adapter with a mass of 20 g was used to concentrate a 2.2 kg mass down to a 3 mm wide distance, which was placed on top of the samples. This experimental setup of the mass and 3D printed adapter resulted in a total mass of

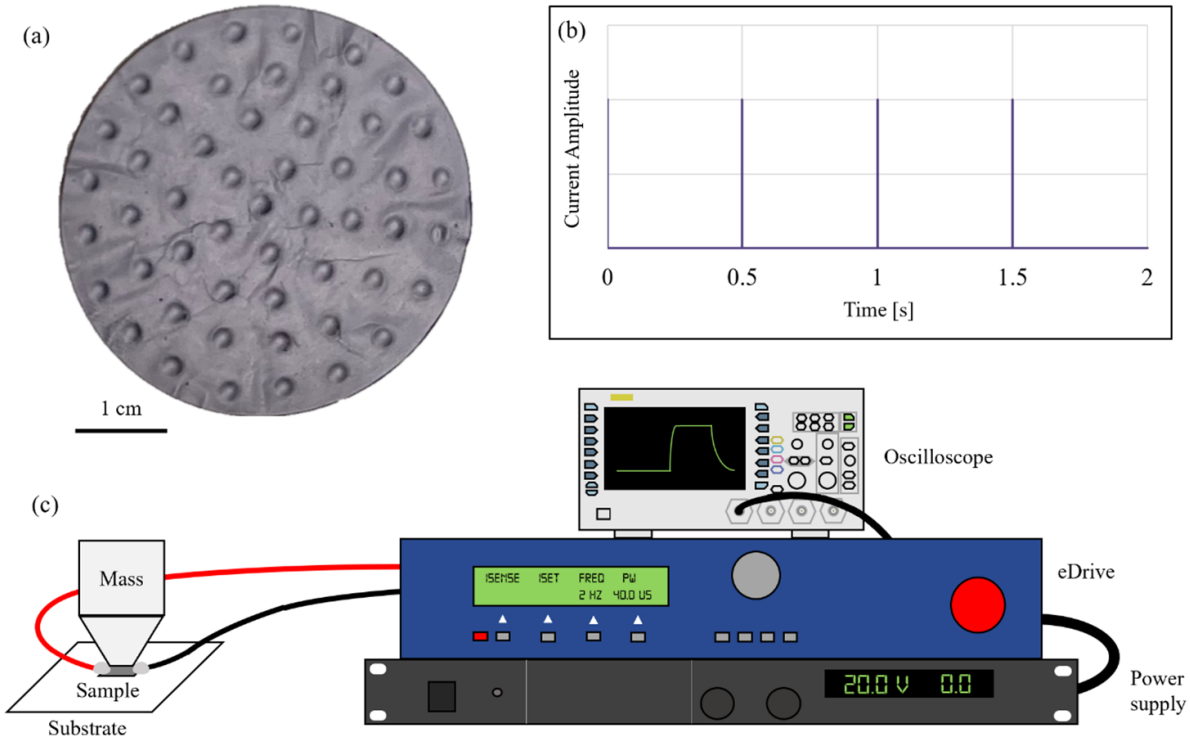

Figure 1. (a) As-received $Ti_3C_2T_x$ MXene film with 500 μm thickness, (b) electropulsing signal generated for electron wind force annealing, and (c) schematic of experimental setup for electron wind force annealing with electropulsing and compressive loading.

2.26 kg that was concentrated down to a 3 mm wide surface. A schematic of the experimental setup for EWF annealing is shown in figure 1(c).

The temperature and thermal changes during electropulsing were measured using an Optris PI 640i thermal infrared (IR) imaging camera. It is important to note that, owing to the compressive loading experiments, the setup obstructed the line of sight, and thermal imaging was not performed. These specimens are expected to exhibit lower temperatures because the force application platform functions as a heat sink. Rigorous temperature mapping was performed for samples that underwent exclusively electropulsing. The experimental setup for exclusively electropulsing was identical to that shown in figure 1(c), with the exception of removing the adapter and mass, and adding the thermal IR camera to record the thermal data. The electrical resistance pre- and post-EWF annealing was determined from the current–voltage (I–V) curve, which was supplied and measured with a Keithley 2400 source measurement unit. The resistance was converted to resistivity by multiplying by the constant cross-sectional area and dividing by the length of the sample. Post-annealing resistivity measurements were performed immediately after annealing and repeated at least 24 h later to determine the time dependence of the EWF annealing process. For all measurements, Kelvin probe connections were used to minimize the contact resistance. Because this EWF annealing process was performed at RT, potential resistivity measurement errors due to thermal expansion or the thermal coefficient of resistivity were avoided.

All specimens in this study were characterized with Raman and x-ray diffraction (XRD) spectroscopy for the crystal structure and phonon vibration. Raman spectroscopy was performed a Horiba LabRam HR Evolution instrument with a 50× long working distance objective and a numerical aperture of 0.5. An average Duoscan spot diameter of 20 μm was utilized to reduce the effective power density of the laser and to increase the measured Raman spectral response. Raman spectral data were obtained using a 785 nm wavelength laser with laser power maintained at approximately 1.7 mW, a 300 gr mm^{-1} grating, and a confocal hole size of 200 μm. Acquisitions were recorded with 60 s integration and three accumulations. Lorentzian peak fitting of the Raman spectral data was performed using the Origin software. A minimum of three locations were recorded for each sample. XRD was performed with an Empyrean III diffractometer (Malvern Panalytical Ltd) using copper (Cu) K-α radiation source. Data was collected in continuous scanning mode at tube voltage of 45 kV and current of 40 mA with a step size of 0.0167°. Further elemental composition investigation was performed with energy dispersive spectroscopy (EDS).

Surface and cross-sectional images of the $Ti_3C_2T_x$ MXene samples were obtained using FIB SEM before and after EWF annealing. Cross-sectional milling was performed using a FEI Helios NanoLab 660 dual-beam SEM with a Gallium ion source. The acceleration voltage of the ion beam was set to 30 kV during milling. Rough milling was performed with a current of 65 nA to remove the material, while polishing of the cross-sectional wall was performed with a current of

2 nA. Surface SEM images were obtained using a typical electron beam at a magnification of 8000×. Cross-sectional SEM images were taken with a typical electron beam at a tilt angle of 52° and a magnification of 20 000×. A tilt-correction feature was utilized to maintain the aspect ratio of the images.

3. Results and discussion

High current density electropulsing with very low duty cycle has been performed on MXene thick films. The core aspect of this process is that the current spikes are too short (20–40 micro-seconds) and sparsely spaced over time (0.5 s) to allow any heat accumulation. Therefore, the specimen temperature remains very close to ambient. This is the major difference in comparison to conventional electro-migration, a damage phenomenon where uncontrollable rise of temperature governs the damage process [24]. In both cases, mechanical stress is generated but there is a significant difference between the basic mechanics in electropulsing and electromigration. In electropulsing, the only source of mechanical stress is the electron-defect interaction. Here, high energy electrons are scattered by the defects and interfaces in materials, resulting in the electrons losing their momentum during the process. The lost momentum essentially imparts mechanical force on the defective atoms. On the other hand, the mechanical stress in electromigration is predominantly thermo-mechanical in nature, where the gradients in temperature field as well as thermal expansion coefficients in heterogeneous materials give rise to the stress [25]. Therefore, it is important to note that this process of electropulsing is a significantly modified version of conventional electromigration that eliminates the temperature field and any thermomechanical stress. The overall effects are, therefore, benign and not damaging.

Table 1 lists the experimental results obtained for the two experimental categories. The samples labeled 'C' denote that external compressive loading was applied during electropulsing, while samples labeled 'E' denote electropulsing with no external loading. Utilizing a synergistic EWF annealing process consisting of electropulsing and compressive loading, a maximum resistivity reduction of 96.65% was achieved at RT. The reduction in resistivity was achieved for sample C1 at a current density of 7.4 A mm^{-2}, after 4 min of EWF annealing. However, it is important to note that with or without external compression, the annealing took place within a few seconds of time. The time vs resistive curve is, therefore, highly non-linear, showing dramatic decrease in resistivity in the first two seconds and rapidly decaying effects thereafter. The scientific explanation behind such behavior is rooted in the difference of the proposed electropulsing and conventional electromigration phenomena. As described earlier, there is no heat accumulation or temperature rise in this process. Hence, the high current density pulses can be thought of as high energy mechanical shock pulses. The first few pulses minimize the defects by reducing their density or reconfiguring them in relation to the direction of current flow, so that they are not as responsive to the remaining current pulses. Therefore, most of the observable effects take place in the first few pulses. Another important finding of this study is that when the post-annealing resistivity measurement was repeated over 24 h later for the same sample, the resistivity increased slightly, but the resulting reduction was still 94% relative to the pre-annealing resistivity. This result indicates that the annealing process was partially, but not completely, permanent. Table 1(a) summarizes the EWF annealing data obtained for this process. It is important to note that the resistivity of the samples much higher than that reported in the literature. This is because most studies have investigated films that are orders of magnitude thinner. For example, specimens thinner than 1 μm show only inter-flake separation as the dominant defect, whereas the 500 microns thick film used in this study showed a very large density of pores with a wide distribution of void size. In table 1, the assignment C denotes the sample that underwent electropulsing and compressive loading. Samples C1–C3 displayed a 90% reduction in resistivity when measured immediately after EWF annealing. However, all the samples displayed a slight increase in resistivity when measured >24 h later, which indicates that the process is not completely permanent and time-dependent. The increase in resistivity from the immediate to repeated measurements varied largely but appeared to be less for the samples that displayed a higher initial resistivity reduction, such as samples C1 and C2.

Table 1(b) displays a summary of the achieved reduction in the resistivity of the samples that underwent the EWF annealing process without any mechanical compression. The maximum resistivity reduction was 78% for sample E1 with a current density of 10.4 A mm^{-2}, after 4 min of annealing. This result is comparable to a previous study, where a 72% resistivity reduction was achieved with a DC current flow with a current density of more than 37 A mm^{-2} [26]. This suggests that a limit on resistivity reduction exists for $Ti_3C_2T_x$ MXene through purely electrical or EWF annealing. This limit was a resistivity reduction in the mid 70% range. As mentioned previously, this reduction can be improved by adding compressive loading. It is important to note that this process is permanent and not time dependent.

An advantage of electropulsing for EWF annealing is that the annealing process can be performed at significantly lower temperatures, as shown in Table 1(b). Figure 2(a) illustrates the maximum temperature of 30.7 °C for sample E1. Figure 2(b) illustrates the maximum temperature of 26.0 °C for sample E2. These samples indicated that the annealing process could be completed at RT. Because the electrical signals for this process and the process including compressive loading are identical and the current densities are very similar, it is safe to assume that the process with compressive loading can also be completed at RT. In contrast, our previous study on annealing via DC yielded a resistivity decrease of approximately 70% at 120 °C [26]. As previously mentioned, $Ti_3C_2T_x$ and other titanium carbide MXenes are oxidized in high-temperature environments in the presence of oxygen. For this reason, the temperature should be minimized during the EWF annealing process under ambient conditions.

Raman analysis with a 785 nm excitation laser provided access to the plasmonic resonance enhanced Raman modes

Table 1. Electrical resistivity data as an indication of annealing effectiveness, (a) electropulsing and compressive loading, and (b) exclusively electropulsing.

(a) Electropulsing with compressive loading

Sample	Pre-annealing resistivity (Ohm m)	Immediate post-annealing resistivity (Ohm m)	Immediate resistivity reduction (%)	Repeated post-annealing resistivity (Ohm m)	Repeated resistivity reduction (%)
C1	3.518×10^{-2}	1.180×10^{-3}	96.65%	1.829×10^{-3}	94.80%
C2	1.252×10^{-2}	5.535×10^{-4}	95.58%	7.518×10^{-4}	94.00%
C3	3.704×10^{-2}	3.299×10^{-3}	91.09%	—	—
C4	1.636×10^{-2}	2.049×10^{-3}	87.48%	5.646×10^{-3}	65.48%
C5	4.120×10^{-2}	7.253×10^{-4}	82.40%	1.003×10^{-3}	75.65%
C6	3.065×10^{-3}	1.141×10^{-3}	62.78%	1.718×10^{-3}	43.93%

(b) Exclusively electropulsing

Sample	Pre-annealing resistivity (Ohm m)	Post-annealing resistivity (Ohm m)	Resistivity reduction (%)	Maximum temperature (°C)
E1	2.367×10^{-3}	5.217×10^{-4}	77.96%	30.7
E2	1.788×10^{-3}	5.369×10^{-4}	69.96%	26.0
E3	2.123×10^{-4}	7.024×10^{-5}	66.91%	27.0
E4	7.372×10^{-5}	3.151×10^{-5}	57.25%	27.2
E5	2.182×10^{-5}	1.030×10^{-5}	52.77%	27.6
E6	9.194×10^{-5}	4.613×10^{-5}	49.83%	29.6
E7	9.577×10^{-4}	4.999×10^{-4}	47.80%	27.0
E8	2.915×10^{-3}	1.561×10^{-3}	46.45%	29.2

ω_1:123 cm^{-1} (E_g, Ti2-C in-plane mode), ω_3:728 cm^{-1} (A_{1g}, C out-of-plane mode), and ω_6:513 cm^{-1} (A_{1g}, T_x out-of-plane mode). Examination of the changes in the Raman spectral response between the as-received MXene and EWF-annealed specimens in figure 2(c) shows that the ω_1 and ω_3 peak maximum positions remain unchanged after annealing. However, the full width at half maximum increased (<0.1 cm^{-1}), as indicated by the small peaks in the residual spectrum. The residual spectrum was the EWF-annealed spectrum minus the original as-received spectrum. The ω_1 and ω_3 peak positions were determined to be sensitive to the type of surface-terminated functional groups. Raman spectroscopy is a well-established technique to identify chemical compounds, and very elaborate 'finger-printing' schemes are available for MXenes [27]. Since the experimental results agree with the literature within the sensitivity of the instrument, it was deduced that there was no modification to the composition of the T_x species due to the EWF annealing. The notable difference in Raman spectroscopy post-EWF annealing is the increase in the relative signal amplitude for the ω_4–ω_7 modes, all of which are associated with T_x vibrations [28]. This relative increase in the signal intensity of the ω_4–ω_7 modes can be attributed to an increase in the T_x concentration within the analyzed volume [27]. A time-dependent study of the as-received MXene specimen, measured one month later, also showed an increase in the ω_4–ω_7 mode intensities, with a $<1/3$ signal increase measured in the EWF-annealed samples. In summary, the changes in the structure and composition of the EWF-annealed MXene samples, as determined by Raman spectroscopy, were minimal, with only a moderate change in the overall T_x concentration.

Surface and cross-sectional FIB SEM images were obtained for the as-received $Ti_3C_2T_x$ MXene, as well as for samples C2 and E1. Five separate locations of cross-sectional SEM images were investigated for each of these three specimens to study the spatial variability. This ensures that a representative set of results can be obtained. Surface images were taken at a magnification of 8000×, whereas cross-sectional images were taken at a magnification of 20 000×.

Surface SEM images are shown in figures 3(a), (d) and (g). Although there is variation in the samples, there is no apparent visual difference in the surface roughness or surface structure after EWF annealing. Because the same samples could not be compared before and post-EWF annealing, an analysis of the internal pore size was performed for each cross-sectional FIB SEM image using ImageJ software and compared to the as-received sample. Justification for such automated image processing includes the speed and accuracy during large volume data analysis. Analyzing the pore characteristics manually would be inaccurate and time-intensive. Numerous cross-sectional SEM images were investigated for this study, while figure 3 only shows a representative example. The cross-sectional FIB SEM images and the corresponding internal pore size distributions can be viewed in figures 3(b), (c), (e), (f), (h) and (i). Cross-sectional images were processed in ImageJ by cropping to a 12–14 μm^2 area of constant illumination, applying a bandpass filter, and thresholding the shades to locate the internal pores, which corresponded to the darkest 13%–15% of shades. The porosity volume fraction for all EWF-annealed samples decreased slightly compared to that of the as-received sample. The as-received sample had a porosity volume fraction of approximately 14.4%, whereas

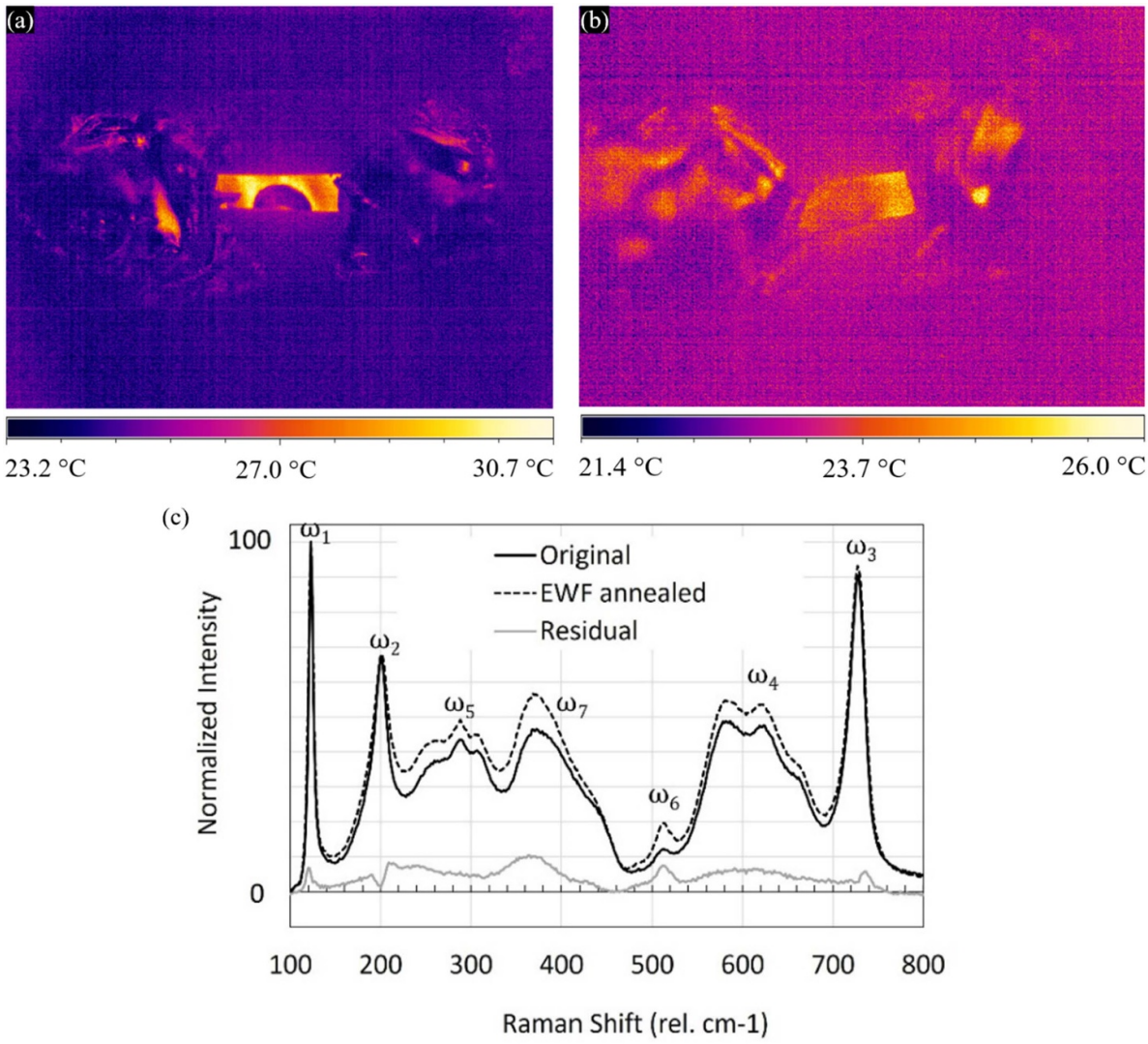

Figure 2. Infrared thermal image of (a) sample E1, (b) sample E2, and (c) Raman spectral averaged response from the original as-received MXene sample compared with the electron wind force (EWF) annealed samples and normalized to the ω_1 resonance peak at 123 cm^{-1}.

sample E2 displayed the lowest porosity volume fraction of 12.1%. Additionally, the average internal pore size for all EWF-annealed samples was lower than that of the as-received sample. The as-received sample displayed an average internal pore size of 2163 N m^2, whereas samples C2 and E1 displayed average internal pore sizes of 1994 N m^2 and 2014 N m^2, respectively. This was also reflected in the normalized frequency histograms of the internal pore sizes for each sample, as shown in figures 3(c), (f) and (i). There is a drastic shift from medium-to large-sized pores in the as-received sample to small pores in the EWF-annealed samples. This was evident based on the normalized frequency of the smallest (<600 N m^2) pore size. For the as-received sample, 26.1% of the pores had an area of <600 N m^2. For the EWF-annealed samples, 38.4–38.8% of the pores displayed an area of <600 N m^2, with the largest percentage coming from sample C2. Generally, there was a decrease in all medium-to large-sized pores from the as-received to EWF-annealed samples, with the largest reduction coming from medium-sized pores with an area of approximately 3000–6000 N m^2. Although there was only a minor change in the porosity volume fraction, it was evident that there was a drastic change in the frequency of nearly all pore sizes, resulting in a smaller average internal pore size after EWF annealing. These results were obtained for a relatively small area under compression (roughly same size as the specimen width). Yet, very consistent results were observed, with resistivity improvements far above the measurement resolution. A future study with increased compression area is, therefore, expected to show better annealing results.

A major motivation for the new annealing process is the ability to reduce electrical resistivity via defect mitigation, while not altering specimen chemical composition. This is an advantage compared to high temperature annealing, where new compounds can be created based on the chemical environment and the temperature. In addition to Raman, XRD spectroscopy as well as EDS were performed. Figures 4 and 5 display the typical signatures of $Ti_3C_2T_x$ MXene when compared to the literature [18, 29, 30]. This clearly indicates that the new

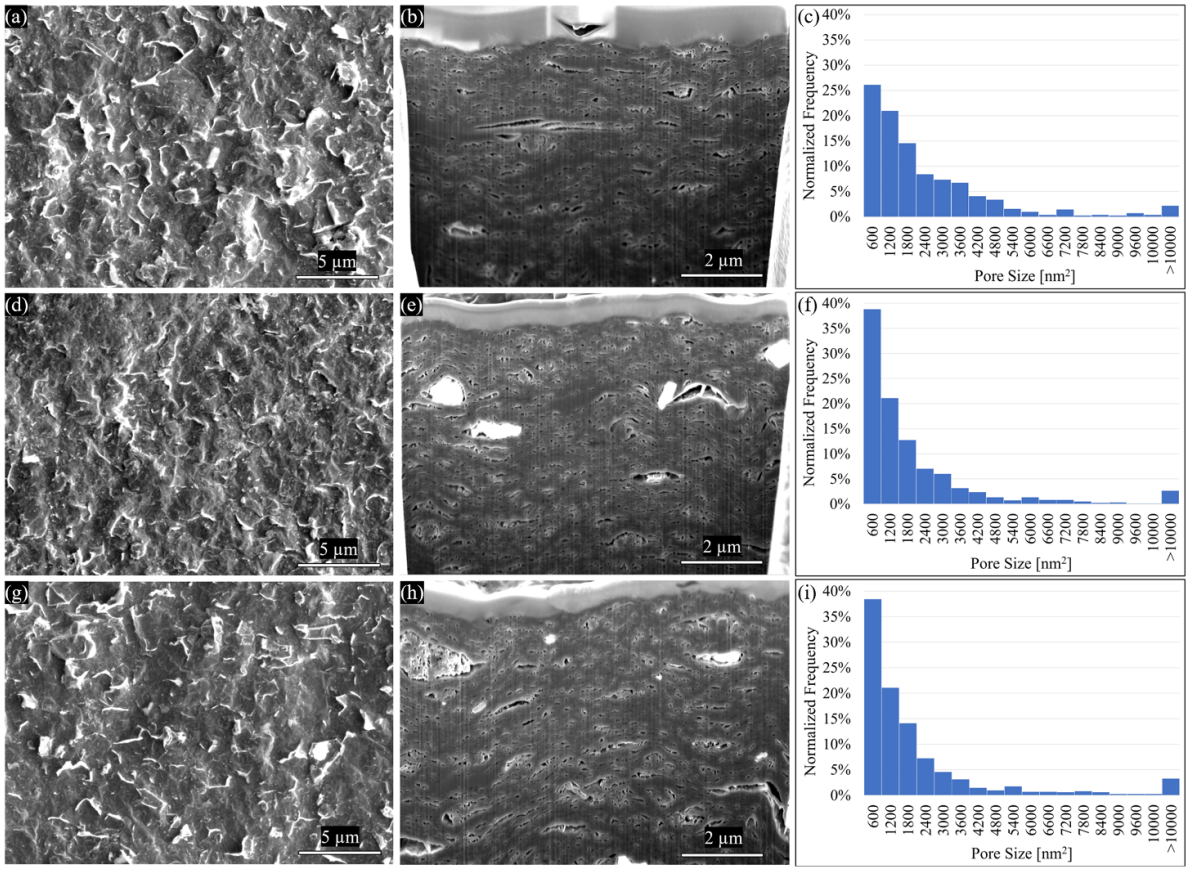

Figure 3. $Ti_3C_2T_x$ surface scanning electron microscope (SEM) image, cross-sectional focused ion beam SEM image, and internal porosity size distribution of, (a)–(c) as-received sample, (d)–(f) sample C2, and (g)–(i) sample E1.

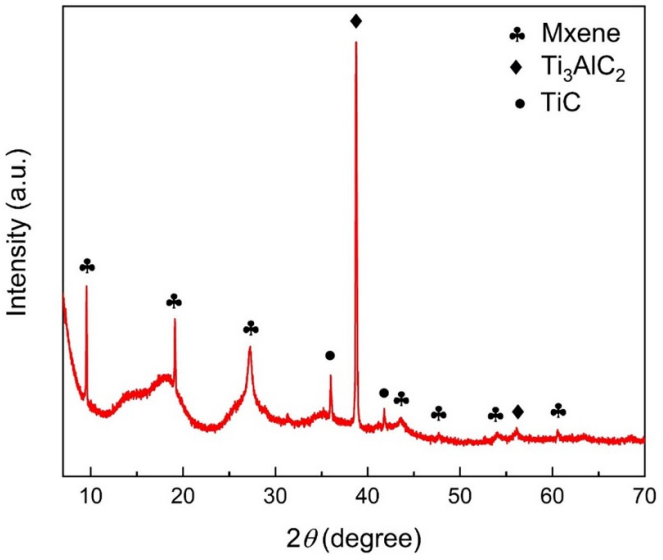

Figure 4. X-ray diffraction (XRD) characterization of the MXene specimen revealing the typical peak signatures.

technique can anneal without any undesired chemical alteration that commonly takes place with high temperature thermal annealing.

To provide a mechanistic understanding of the effect of external compressive load on the EWF annealing, three core aspects of the problem can be noted: (a) the large spread in the pore size and shape in the as-received MXene, (b) EWF is highly inhomogeneous in spatial sense, and (c) EWF annealing is very effective in mobilizing defective atoms ~~as~~ in one or 2D defects (such as interface), but it may not produce enough magnitude of forces to mobilize 3D or microscopic pores. The first aspect is schematically shown in figure 6, where the spectrum of defects starts at the atomic scale with interfaces between nanoscale flakes. These defects are essentially surface-type and not visible with SEM imaging or unless atomically resolved. The other end of the spectrum has micron sized pores. The size and shape of defects influence the effectiveness of EWF, which is inherently inhomogeneous in nature. This is the second core aspect of the problem; EWF originates only when the electrons encounter defects or interfaces. It is important to note the difference between the homogeneity of electron-lattice scattering that gives rise to Joule heating (intentionally suppressed in this study as mentioned earlier). This makes the EWF a highly inhomogeneous or defect-specific force in nature [31]. In addition, EWF is also influenced by the inhomogeneity arising from shape of the pores. A lenticular or elliptical pore may induce more current crowding (and hence higher magnitude of EWF) compared to a circular pore [32].

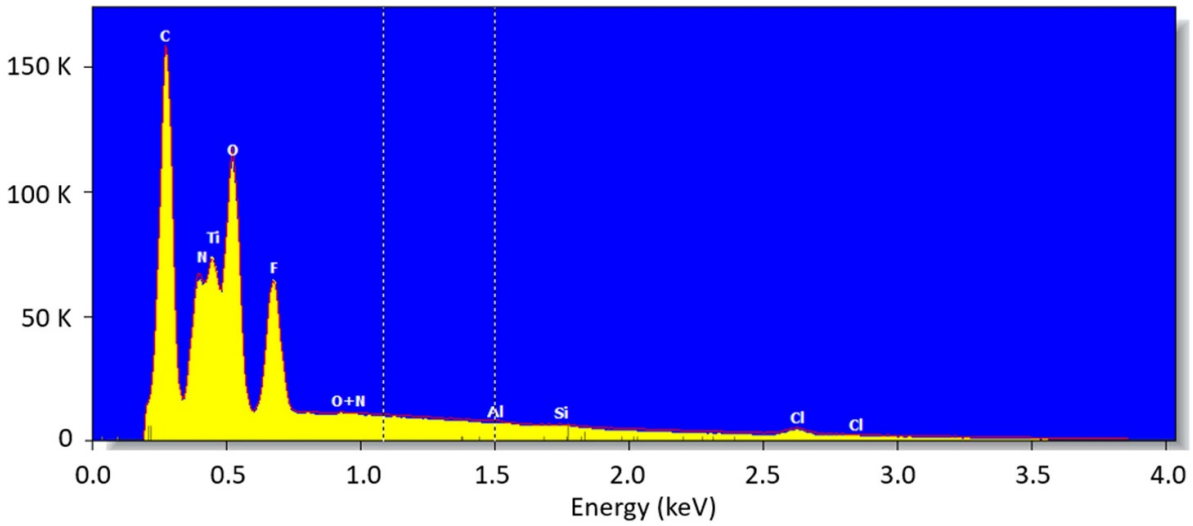

Figure 5. Elemental composition characterization with energy dispersive spectroscopy.

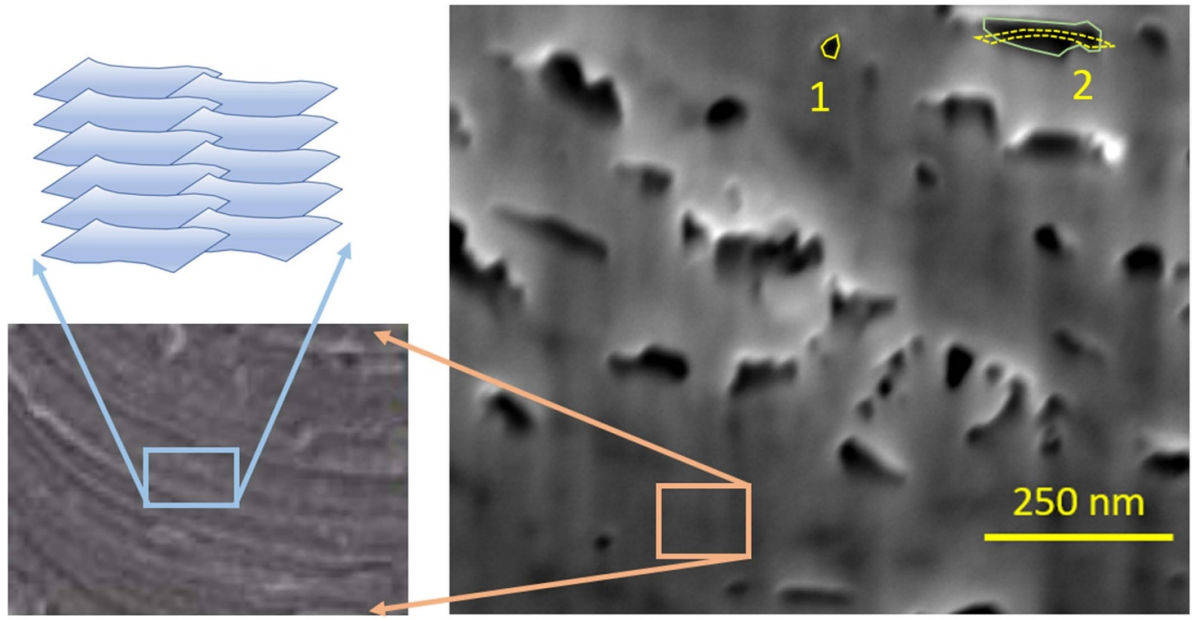

Figure 6. SEM images and schematic diagram showing multi-scale nature of the defects in thick MXene films. Type 1 defects are non-compliant, while type 2 defects are compliant and thus responsive to external mechanical stress. Dashed lines show the closing of type 2 compliant defects under external mechanical compressive stress. Reproduced from [33]. CC BY 4.0.

We propose that without any externally applied compressive force, the EWF annealing is most effective at minimizing atomic scale defects, such as interfaces between the MXene nanoflakes. These are shown in relatively solid-resembling areas in a low magnification cross-sectional view in figure 6. The EWF magnitude may not be large enough to mobilize defects of larger length-scale. This is where external compressive force is helpful. For very high aspect ratio defects (labeled as type 2 in figure 6) the structural compliance is also high, and the compressive force can bring the surfaces in contact (resembling an interface between two layers of solids) as shown by the dashed line. Under the influence of external compression, EWF is very effective on these defects because their surfaces can be brought to close contact while the current is passed through the specimen. For low aspect ratio micropores, (labeled as type 1 in figure 6), the compliance is very low. Therefore, these pores do not close under the external force and are also not responsive to the EWF annealing (with or without external compression). This is why the smallest micropores (visible through SEM imaging) do not decrease in population, whereas there is appreciable decrease in the density of larger, more compliant pores. It is important to note that mechanical stress significantly influences both electromigration and EWF phenomena. In particular, compression has been shown to reduce the extent of electromigration damage [34], which can be interpreted as a positive influence for this study. Finally, it should be noted that the proposed conceptual mechanisms are mostly fundamental in nature and cannot be used

to ascertain deviations from the idealness of any experiments. For example, only high-fidelity simulations can account for the exact size and shape of the defects as well as the mathematical complexity (nonlinear as well as spatially inhomogeneous) of the current density effects on electromigration and electropulsing [24]. Similarly, a potential non-parallel compressive field (such as mis-aligned compressive load) would still compress a type 2 (figure 6) defect albeit to a lesser extent. Since the type 2 defects are seen to be randomly distributed in the thick film, the effect of any slight misalignment in the direction of compression may not have prominent effect.

4. Conclusion

The outstanding properties of MXenes reported in the literature are due to the length-scale of the specimen. For example, nanosheet specimens exhibit inter-layer or flake-separation-type defects. On the other hand, MXenes that would be necessary for micro-engineering applications are an order of magnitude thicker, and as shown in this study, exhibit a predominance of pores with a large spread in size. Therefore, the key annealing mode in thicker films is the elimination of void-type defects. The core theme of this study is that compressive loading can be highly effective when applied synergistically with electrical pulses. It has been demonstrated that EWF annealing with electropulsing and compressive loading can achieve >90% reduction in the electrical resistivity of $Ti_3C_2T_x$ MXene. This reduction could likely be further improved by optimizing both electropulsing and compressive parameters.

The resistivity reductions in this study were primarily achieved by reducing the (a) interfacial defects for nano-flakes and (b) density of larger and higher aspect ratio pores that are structurally compliant to any external compressive load. Internal porosity analysis of FIB SEM cross-sectional images performed in ImageJ showed a reduction in both the average pore size and porosity volume fraction, with the most significant change being a reduction in pore size. After EWF annealing, the frequency of smaller pores (<600 N m^2) increased significantly, while the frequency of nearly all other pore sizes decreased after EWF annealing. The reduction in pore size can likely be attributed to the magnitude of the current density and current detour effect. Finally, the Raman spectra showed no major changes in the $Ti_3C_2T_x$ composition. Considering that this annealing process took place at room temperature, changes in composition or reductions in surface terminations were not expected. In other words, this new annealing process improves the properties of MXene without affecting its intrinsic chemistry and microstructure. This demonstration of low temperature defect control can potentially impact MEMS sensor and energy applications for improved performance.

Data availability statement

The data that support the findings of this study are available upon reasonable request from the authors.

Acknowledgments

The authors acknowledge support from the Division of Civil, Mechanical, and Manufacturing Innovation (Nanomanufacturing program) of the National Science Foundation (NSF) through award #1760931. The authors also acknowledge support from the Division of Materials Research, Metal & Metallic Nanostructure Program through award #2103928.

Ethical compliance

This study did not involve human participants, animals or biomaterials.

Conflict of interest

The authors declare that they have no affiliations with or involvement in any organization or entity with any financial interest in the subject matter or materials discussed in this manuscript.

ORCID iDs

Maxwell Wetherington https://orcid.org/0000-0003-1958-1354
Aman Haque https://orcid.org/0000-0001-6535-5484

References

[1] Murali G, Reddy Modigunta J K, Park Y H, Lee J-H, Rawal J, Lee S-Y, In I and Park S-J 2022 A review on MXene synthesis, stability, and photocatalytic applications *ACS Nano* **16** 13370–429
[2] Zhang Z, Yao Z, Zhang X and Jiang Z 2020 2D Carbide MXene under postetch low-temperature annealing for high–performance supercapacitor electrode *Electrochim. Acta* **359** 136960
[3] Aslam M K, Niu Y and Xu M 2021 MXenes for non-lithium-ion (Na, K, Ca, Mg, and Al) batteries and supercapacitors *Adv. Energy Mater.* **11** 2000681
[4] Zhao Q, Zhu Q, Liu Y and Xu B 2021 Status and prospects of MXene-based lithium–sulfur batteries *Adv. Funct. Mater.* **31** 2100457
[5] Kang H , Wang J F, Wang Y D, Liu Y Y, Fan Z M, Xie Z M and Cheng Z J 2021 Research progress in $Ti_3C_2T_x$ MXene-based electromagnetic interference shielding material *J. Mater. Sci.* **49** 14–25
[6] Iqbal A, Sambyal P and Koo C M 2020 Electromagnetic interference shielding: 2D MXenes for electromagnetic shielding: a review *Adv. Funct. Mater.* **30** 2070307
[7] Han M, Liu Y, Rakhmanov R, Israel C, Tajin M A S, Friedman G, Volman V, Hoorfar A, Dandekar K R and Gogotsi Y 2021 Solution-processed $Ti_3C_2T_x$ MXene antennas for radio-frequency communication *Adv. Mater.* **33** 2003225
[8] Al-Hamadani Y A J, Jun B-M, Yoon M, Taheri-Qazvini N, Snyder S A, Jang M, Heo J and Yoon Y 2020 Applications of MXene-based membranes in water purification: a review *Chemosphere* **254** 126821
[9] Zhang D, Shah D, Boltasseva A and Gogotsi Y 2022 MXenes for photonics *ACS Photonics* **9** 1108–16

[10] Li N, Peng J, Ong W-J, Ma T, Zhang P, Jiang J, Yuan X and Zhang C J 2021 MXenes: an emerging platform for wearable electronics and looking beyond *Matter* **4** 377–407
[11] Jiang Q, Kurra N, Maleski K, Lei Y, Liang H, Zhang Y, Gogotsi Y and Alshareef H N 2019 On-chip MXene microsupercapacitors for AC-line filtering applications *Adv. Energy Mater.* **9** 1901061
[12] Wang C, Li R, Feng L and Xu J 2022 The SnO_2/MXene composite ethanol sensor based on MEMS platform *Chemosensors* **10** 109
[13] Ma Y, Liu N, Li L, Hu X, Zou Z, Wang J, Luo S and Gao Y 2017 A highly flexible and sensitive piezoresistive sensor based on MXene with greatly changed interlayer distances *Nat. Commun.* **8** 1–8
[14] Cai Y, Shen J, Ge G, Zhang Y, Jin W, Huang W, Shao J, Yang J and Dong X 2018 Stretchable $Ti_3C_2T_x$ MXene/carbon nanotube composite based strain sensor with ultrahigh sensitivity and tunable sensing range *ACS Nano* **12** 56–62
[15] Nguyen V H, Tabassian R, Oh S, Nam S, Mahato M, Thangasamy P, Rajabi-Abhari A, Hwang W-J, Taseer A K and Oh I-K 2020 Stimuli-responsive MXene-based actuators *Adv. Funct. Mater.* **30** 1909504
[16] Zhao X, Wang Z, Dong J, Huang T, Zhang Q and Zhang L 2020 Annealing modification of MXene films with mechanically strong structures and high electrochemical performance for supercapacitor applications *J. Power Sources* **470** 228356
[17] Xu H, Yin X, Li X, Li M, Zhang L and Cheng L 2019 Thermal stability and dielectric properties of 2D Ti_2C MXenes via annealing under a gas mixture of Ar and H_2 atmosphere *Funct. Compos. Struct.* **1** 015002
[18] Wyatt B C, Nemani S K, Desai K, Kaur H, Zhang B and Anasori B 2021 High-temperature stability and phase transformations of titanium carbide ($Ti_3C_2T_x$) MXene *J. Phys.: Condens. Matter* **33** 224002
[19] Wozniak J, Petrus M, Cygan T, Lachowski A, Kostecki M, Jastrzębska A, Wojciechowska A, Wojciechowski T and Olszyna A 2021 Investigation of MXenes oxidation process during sps method annealing *Materials* **14** 6011
[20] Lee Y, Kim S J, Kim Y-J, Lim Y, Chae Y, Lee B-J, Kim Y-T, Han H, Gogotsi Y and Ahn C W 2020 Oxidation-resistant titanium carbide MXene films *J. Mater. Chem.* A **8** 573–81
[21] Hart J L, Hantanasirisakul K, Lang A C, Anasori B, Pinto D, Pivak Y, van Omme J T, May S J, Gogotsi Y and Taheri M L 2019 Control of MXenes' electronic properties through termination and intercalation *Nat. Commun.* **10** 522
[22] Persson I *et al* 2018 On the organization and thermal behavior of functional groups on Ti_3C_2 MXene surfaces in vacuum *2D Mater.* **5** 015002
[23] Hill C, Jones S and Boys D 1989 Rapid thermal annealing—theory and practice *Reduced Thermal Processing for ULSI* ed R A Levy (Boston, MA: Springer) pp 143–80
[24] De Orio R, Ceric H and Selberherr S 2010 Physically based models of electromigration: from black's equation to modern TCAD models *Microelectron. Reliab.* **50** 775–89
[25] Yao W and Basaran C 2013 Computational damage mechanics of electromigration and thermomigration *J. Appl. Phys.* **114** 103708
[26] Rasel M A J, Wyatt B, Wetherington M, Anasori B and Haque A 2021 Low-temperature annealing of 2D $Ti_3C_2T_x$ MXene films using electron wind force in ambient conditions *J. Mater. Res.* **36** 3398–406
[27] Sarycheva A and Gogotsi Y 2020 Raman spectroscopy analysis of the structure and surface chemistry of $Ti_3C_2T_x$ MXene *Chem. Mater.* **32** 3480–8
[28] Hu T, Wang J, Zhang H, Li Z, Hu M and Wang X 2015 Vibrational properties of Ti_3C_2 and $Ti_3C_2T_2$ (T = O, F, OH) monosheets by first-principles calculations: a comparative study *Phys. Chem. Chem. Phys.* **17** 9997–10003
[29] Wang H, Wu Y, Zhang J, Li G, Huang H, Zhang X and Jiang Q 2015 Enhancement of the electrical properties of MXene Ti_3C_2 nanosheets by post-treatments of alkalization and calcination *Mater. Lett.* **160** 537–40
[30] Wang X, Fan X, Li M, Zhu W, Xue J, Ye F and Cheng L 2021 Structure and electromagnetic properties of $Ti_3C_2T_x$ MXene derived from Ti_3AlC_2 with different microstructures *Ceram. Int.* **47** 13628–34
[31] Zhao Z, Mamidanna A, Lefky C, Hildreth O and Alford T L 2016 A percolative approach to investigate electromigration failure in printed Ag structures *J. Appl. Phys.* **120** 125104
[32] Arzt E, Kraft O, Nix W D and Sanchez J E 1994 Electromigration failure by shape change of voids in bamboo lines *J. Appl. Phys.* **76** 1563–71
[33] Yin J, Pan S, Guo X, Gao Y, Zhu D, Yang Q, Gao J, Zhang C and Chen Y 2021 Nb_2C MXene-functionalized scaffolds enables osteosarcoma phototherapy and angiogenesis/osteogenesis of bone defects *Nano-Micro Lett.* **13** 30
[34] Chang H H, Su Y F, Liang S Y and Chiang K N 2015 The effect of mechanical stress on electromigration behavior *J. Mech.* **31** 441–8